LUND UNIVERSITY

Extraction of tissue optical properties from optical coherence tomography images for diagnostic purposes

Thrane, L; Frosz, MH; Levitz, D; Jorgensen, TM; Andersen, CB; Hansen, PR; Valanciunaite, J; Swartling, Johannes; Andersson-Engels, Stefan; Tycho, A; Yura, HT; Andersen, PE

Link to publication

LUND UNIVERSITY

PO Box 117
221 00 Lund
+46 46-222 00 00

Extraction of tissue optical properties from optical coherence tomography images for diagnostic purposes

Lars Thrane[a], Michael H. Frosz[a,b], David Levitz[a,c], Thomas M. Jørgensen[a], Claus B. Andersen[d], Peter R. Hansen[e], Jurga Valanciunaite[c], Johannes Swartling[c], Stefan Andersson-Engels[c], Andreas Tycho[f], Harold T. Yura[g], and Peter E. Andersen*,[a]

[a]Optics and Plasma Research Department, Risø National Laboratory, P.O. Box 49, DK-4000 Roskilde, Denmark
[b]COM, Technical University of Denmark, DTU- Building 345V, DK-2800 Kgs. Lyngby, Denmark
[c]Department of Physics, Lund Institute of Technology, P.O. Box 118, SE-221 00 Lund, Sweden
[d]Department of Pathology, Rigshospitalet, Frederik V's vej 11, DK-2100 København Ø, Denmark
[e]Department of Cardiology, Amtssygehuset i Gentofte, Niels Andersensvej, DK-2900 Hellerup, Denmark
[f]OCT Innovation ApS., P.O. Box 49, DK-4000, Roskilde, Denmark
[g]Electronic and Photonics Laboratory, The Aerospace Corporation, P.O. Box 92957, Los Angeles, CA 90009 USA

ABSTRACT

The concept of optical coherence tomography (OCT) for high-resolution imaging of tissues in vivo is introduced. Analytical and numerical models for describing and understanding the light propagation in samples imaged by OCT systems are presented. An analytical model for calculating the OCT signal based on the extended Huygens-Fresnel principle and valid both for single and multiple scattering regimes is outlined. From this model, an algorithm for extracting tissue optical properties for multi-layered tissues is derived. The algorithm is first verified for various optical properties and geometries using solid phantoms and numerical simulations. The applicability of the algorithm for extraction of tissue optical properties is then demonstrated for vascular tissue samples *ex vivo*. With the use of data from numerical phantoms, the validity of the OCT extraction algorithm for a two-layer geometry is further supported. It is concluded that by using optical properties extracted from OCT images of human tissues, the clinical utility of OCT imaging can be substantially increased.

Keywords: optical coherence tomography, tissue optical properties, scattering

1. INTRODUCTION

Optical coherence tomography (OCT) is a non-invasive technique that provides micron-scale imaging of tissue.[1] OCT is driven by low-coherence interferometry, an interferometric method whereby an interference signal can only arise when the optical path length difference between the two arms of a Michelson interferometer is within the coherence length of the source. Thus in OCT the axial resolution is proportional to the temporal coherence length of the source, and with a broadband source it is possible to obtain a resolution as high as 0.5 μm in tissue.[2] As a fiber-based technology, OCT can be readily integrated into many catheter-based endoscopic applications.[3]

However, one major problem preventing OCT from being more readily integrated into the diagnostic armamentarium is the lack of methods for objective interpretation of tissue morphology in OCT images. OCT signals are mainly influenced by the optical properties of the examined sample, that is, the scattering coefficient μ_s and anisotropy factor g[4]. They are macroscopic physical properties unique to the tissue, which play a vital role in the modeling of OCT signals. By properly modeling an OCT signal as a function of depth so that multiple scattering events are included, and fitting the depth profile of coherent backscattered light in an OCT image (also called depth-scan or A-scan) to such model, it is possible to extract out μ_s and g, which in turn enable new diagnostic methods. The principal aim of this paper is to present this novel new method by which optical properties data can be extracted from OCT images.

Our objectives in this study were as follows: Firstly, to demonstrate that the curve-fitting algorithm used was capable of accurately determining the optical properties of turbid media. This evaluation part of the study was conducted

on a set of tissue phantoms using integrating sphere measurements to determine optical scattering properties.[5] Secondly, the OCT extraction method was applied on normal and atherosclerotic human aortic samples in order to demonstrate that the technique may provide a basis for distinguishing between different tissues by their optical properties.[5] Thirdly, the modeling geometry is extended to include a second layer and verified the ability of the algorithm to extract the optical properties of both layers using a numerical phantom.[6]

2. OCT SYSTEM AND THEORETICAL MODELING

Throughout this study, OCT data curves were fit to an analytical OCT model. These curves were either generated experimentally, i.e., by OCT imaging (single-layer studies), or by numerical simulation, i.e., using Monte Carlo simulations (two-layer study). The principal equations governing the OCT signal for both cases were the same,[9] and are presented in Section 2.1. However, because of the differences in the nature of data collected between the two systems, different preprocessing steps were needed before curve fitting was carried out. In Section 2.2 details regarding the OCT imaging and the extraction algorithm used to process OCT images are provided,[5] while in Section 2.3 we explain how data generated using our numerical OCT model were processed.[6,7]

2.1 Analytical OCT model

A model based on the extended Huygens-Fresnel principle[8] that analyzes the heterodyne OCT signal as a function of depth has been developed by Thrane et al.[9] (denoted EHF model). This model takes into account multiple scattering effects, and thus the depth profile of the OCT signal is a function of μ_s and g as well as other parameters. This model is based on ABCD matrix formalism[10] and is therefore general and capable of handling different sample arm geometries, i.e., dynamic vs. fixed focusing. Furthermore, it may easily be applied to a multiple-layered geometry of scattering media, such as is frequently the case with tissue.

The analytical expressions for the OCT signal of the two layers are obtained from the general expression given by Eq. (22) of Ref. 9

$$\langle i^2(z) \rangle = \langle i^2 \rangle_0 \left[\exp(-2\mu_s z) + \frac{4\exp(-\mu_s z)\left[1-\exp(-\mu_s z)\right]}{1+w_S^2/w_H^2} + \left[1-\exp(-\mu_s z)\right]^2 \frac{w_H^2}{w_S^2} \right], \tag{1}$$

where $\langle i^2(z) \rangle$ and $\langle i^2 \rangle_0$ is the mean square heterodyne signal current in the presence and absence of scattering, respectively, and z is the probing depth. Note that the OCT signal is the root mean square (rms) heterodyne signal current $\sqrt{\langle i^2(z) \rangle}$. The quantities w_H and w_S are the $1/e$ intensity radii at the probing depth in the absence and presence of scattering, respectively, defined as

$$w_H^2 = w_0^2 \left(A - \frac{B}{f} \right)^2 + \left(\frac{B}{kw_0} \right)^2, \tag{2}$$

$$w_S^2 = w_0^2 \left(A - \frac{B}{f} \right)^2 + \left(\frac{B}{kw_0} \right)^2 + \left(\frac{2B}{k\rho_0(z)} \right)^2, \tag{3}$$

with w_0 being the $1/e$ intensity radius of the reference and input sample beams in the lens plane/mixing plane, and A and B are the ray-matrix elements. $\rho_0(z)$ is the lateral coherence length in the mixing plane of the sample field that has been reflected/backscattered at the probing depth z. A derivation of $\rho_0(z)$[9,11] shows that

$$\rho_0(z) = \sqrt{\frac{3}{\mu_s z}} \frac{\lambda}{\pi\theta_{rms}} \left(\frac{nB}{z} \right), \tag{4}$$

where θ_{rms} represents the root-mean-square scattering angle, defined as the half-width at e^{-1} maximum of a Gaussian curve fit to the main frontal lobe of the scattering phase function[12]. Strictly speaking, the anisotropy parameter extracted, g_{eff}, is the effective anisotropy factor given by the cosine of θ_{rms} found in Eq. 4.

Eqs. (1-4) are the underlying equations on which are fitting algorithm is based on. Note that in the OCT system used in this phantom and tissue study, light was focused at the surface of the sample and thus A = 1 and B = f + (z / n). However, in the Monte Carlo model is based on a system employing dynamic focusing, i.e., B = f. Consequently, in this

case $\left\langle i^2 \right\rangle_0$ is a constant proportional to the effective backscattering cross section of the sample, and $w_H^2 / w_s^2 = \left\{ 1 + \left[2w_0 / \rho_0 (z) \right]^2 \right\}^{-1}$, according to Ref. 9.

2.2 OCT imaging and image processing

This section describes the system used to acquire OCT data (Subsection 2.2.1), and the steps taken to get from a two-dimensional matrix of intensity values to a set of optical property values that best described the OCT signal over the specified region of interest (Subsection 2.2.2).

2.2.1 OCT system

The OCT system used for this study (Fig. 1) employed a broadband source with a center wavelength of 1300 nm (AFC, Inc., model BBS 1310), providing a subsequent axial resolution of ~10 μm in tissue. The sample arm unit consisted of a handheld probe that the user holds in contact with the sample. A computer-controlled transverse scanning module and an integrated digital video camera were incorporated into the probe unit. The digital video camera was used to visually assist transverse scanning. In the reference arm, fast scanning was achieved with use of a Fourier domain rapid-scanning optical delay line[13]. An InGaAs (New Focus, Inc., model 2017) detector measured the interference pattern between the two arms of the interferometer. During the first part of the study, an optical circulator between the source and the 50/50 beam splitter was included in the setup, which was also connected to a second detector to allow for dual balanced detection that increased signal-to-noise ratio (SNR)[14]. The electronic signal emerging from the detector was amplified and high-pass filtered. Detection of the interferometric envelope was implemented in hardware using a programmable logic device. Thereafter, the signal was digitized and stored on a computer.
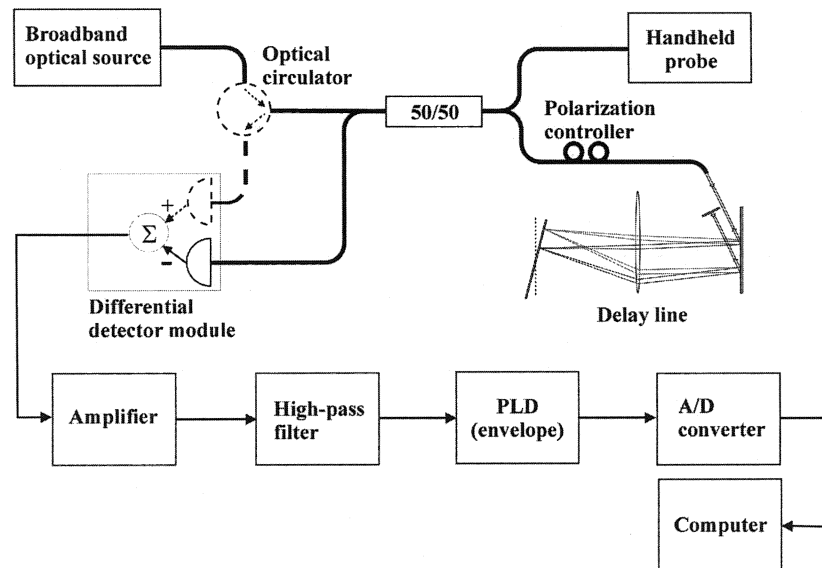

Fig. 1: The OCT system. The optical circulator and a second detector (dashed line) were only used in the first part of the study. PLD: programmable logic device. Adopted from Ref. 5.

The OCT system was used to capture depth interferometric information from the investigated samples resulting in images with 690 axial (z) pixels (4.16 μm spacing) and 400 transverse (x) pixels (10 μm spacing). In all the images, light was focused on the surface of the scattering medium. Corresponding digital photographs of the sample and the scanned region were automatically taken along with every OCT image. Image acquisition time from start of scanning was 5-6 seconds. The dynamic range of the system was >100 dB.

2.2.1 OCT image processing algorithm

We have developed an algorithm based on Eqs. (1-4) consisting of a set of Matlab codes for the purpose of mathematically processing OCT images.[5] The principles of how optical scattering properties are evaluated from a given

image are illustrated in Fig. 2. Fig. 2(A) shows a detailed geometry of the sample arm unit during measurements, and Fig. 2(B) presents a typical raw OCT image of a tissue phantom. First, the user selected a transverse region of interest (ROI, orange dashed inset in Fig. 2(B)) from a given image, consisting of several adjacent depth-scans. These adjacent A-scans were averaged along the lateral direction and smoothed as shown in Fig. 2(C). The number of longitudinal pixels to which the model would be fit to was chosen from this curve (dashed inset in Fig. 2(C)), with pixels representing the specular reflection excluded. Finally, Fig. 2(D) shows a comparison of data points fit to $\sqrt{\langle i^2(z) \rangle}$, returned along with the scattering coefficient μ_s, the root-mean-square scattering angle, θ_{rms} ($g_{eff} = \cos \theta_{rms}$), and error estimates.
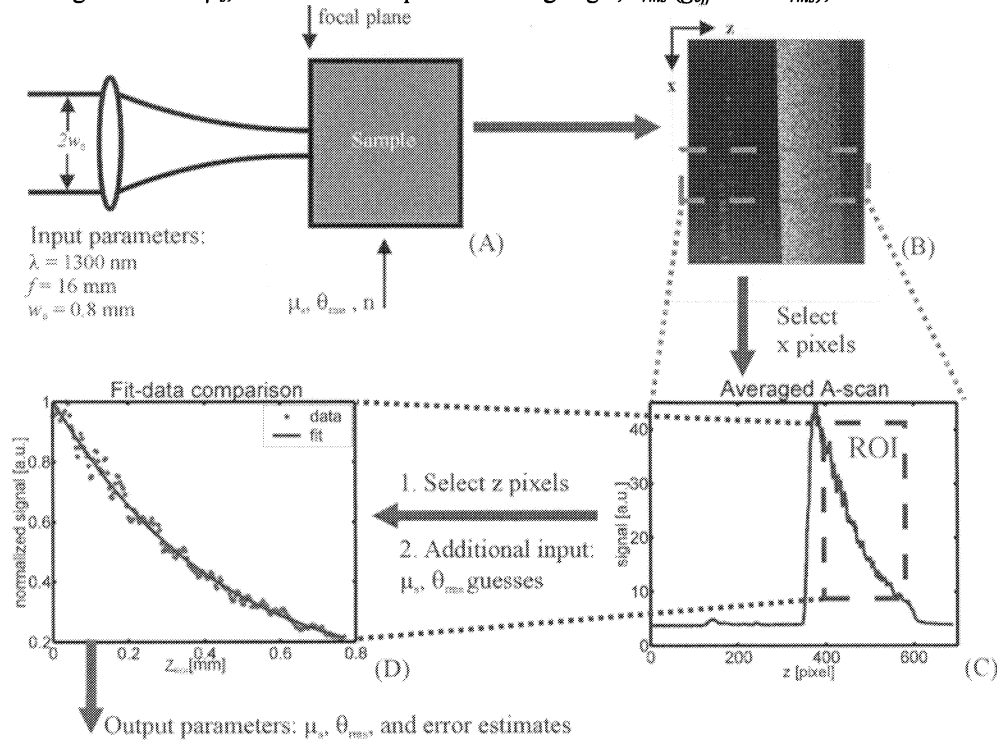

Fig. 2: A schematic representation of the principles of the extraction algorithm. The sample arm geometry and input parameter values from our OCT setup are shown in (A). These parameters were used to generate an image (B) and were also employed during curve fitting (C-D). A transverse ROI was selected in (B, inset), averaged, smoothed, and plotted in (C). The axial pixels of the ROI were chosen in (C, inset), and shown as points in (D). z_{ROI} represents the probing depth within the region of interest in (D). The fit was performed on the resulting data-points using μ_s and θ_{rms} initial value guesses as additional input. The algorithm returned μ_s, θ_{rms}, the fit's error estimates, and a plot comparing the fit to the data points (D). Adopted from Ref. 5.

2.3 Numerical OCT model and subsequent processing

In the verification of our ability to extract optical properties from multi-layered structures, we used the Monte Carlo (MC) OCT model developed by Tycho et al.[7] to create a numerical phantom, i.e., to simulate the OCT signal from a two-layer tissue structure. A layer was defined as a plane-parallel homogeneous region characterized by a scattering coefficient μ_s, an anisotropy factor g_{eff}, and an index of refraction n. Each numerical simulation resulted in a single signal value at a particular probing depth; thus, an OCT data curve required several simulation runs. We then fitted the two-layer EHF expression for the OCT signal to the MC simulated signal, extracted the optical scattering properties μ_s and g_{eff} (and μ_a) of each of each medium in question, and compared them with the MC input values. Because the scattering phase function used in both the EHF and MC OCT models were Gaussian, we could directly compare the extracted g_{eff} values with the MC input g_{eff} values. Note that no processing was carried out on the $\sqrt{\langle i^2(z) \rangle}$ data points prior to fitting.
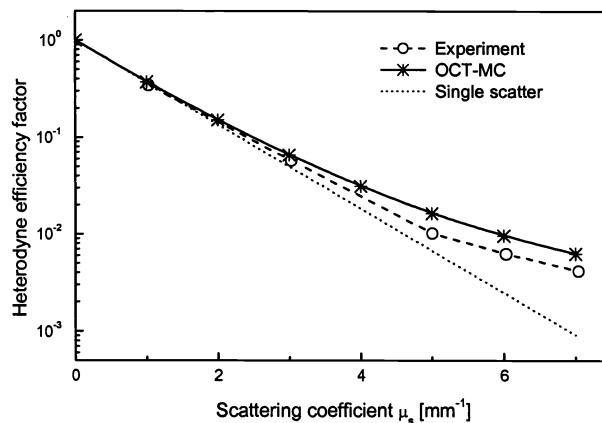
Fig. 3: The heterodyne efficiency factor as a function of μ_s for a fixed probing depth (0.5 mm) in a homogeneous sample obtained by using the MC OCT model, and with data from experiments presented elsewhere[9]. The typical standard deviation for the measurements (O) was ±7.8%. The dotted curve represents the predicted single-scattering OCT model[15] ($\lambda = 814$ nm, $g = 0.929$ ($\theta_{rms} = 0.38$ rad), $n = 1.33$, $f = 16$ mm, $w_0 = 0.125$ mm). Adopted from Ref. 6.

The applied MC OCT model[7] is an extension of the well-known MCML computer code,[16] which allows simulation of multi-layered media. As shown in Fig. 3, there was excellent agreement between results obtained for the heterodyne efficiency factor[7] as a function of μ_s for a fixed probing depth by using the MC OCT model and data from experiments presented elsewhere[9], indicating that the MC model was a valid model of the data generated by OCT. Thus, the MC OCT model used in this work represents a valid numerical OCT phantom and a powerful investigational tool in the analysis of OCT data.

3. SINGLE-LAYER PHANTOM STUDY

In order to establish the reliability of our new algorithm for extracting optical properties of highly scattering media, experiments on tissue phantoms with well-controlled optical properties were carried out. Specifically, this verification involved several phantoms with different scattering properties measured with a well-established method for obtaining optical properties from such samples, i.e., the integrating sphere method and inverse adding-doubling (IAD)[17]. To adequately compare the extracted g_{eff} values, the scattering phase function of 1300 nm light in those phantoms was calculated using basic principles from Mie theory.[4]

3.1 Phantoms

For these experiments, we used six phantoms from a previous investigation[18] with three distinct values of μ_s and two distinct values of absorption coefficient μ_a, respectively. The phantoms consisted of epoxy resin (n=1.55) with well-defined quantities of scattering material and absorbing pigment added for scattering and absorption purposes, respectively. Titanium IV Oxide (TiO$_2$, n=2.55) powder, with a particle size of 1 μm (Sigma-Aldrich) was used as a scattering material and photocopy machine toner served as the absorbing pigment. In all phantoms used, it was ensured that absorption effects were negligible compared to those from scattering. Mounting the phantoms in a slab geometry was achieved by sandwiching 1 ml of each phantom between two microscope slides before the epoxy hardened yielding 1.0 mm thick samples with a cross section measuring 3 x 3 cm^2.[18]

3.2 Integrating sphere measurements

Our measurements of the diffuse reflectance and transmittance were performed using an integrating sphere (Labsphere model RT-060-SF) with the broadband source (AFC) operating at a center wavelength of 1300 nm also used for OCT imaging. Light was guided to the sphere using a single-mode optical fiber and collected by an IR detector supplied by the sphere manufacturer. The beam arriving at the transmission port was 2.3 mm in diameter, with a port diameter of 25.4 mm. A chopper rotating at 730 Hz modulated the beam, and was synchronized with a lock-in amplifier on the detector side to increase SNR. Both diffuse reflectance and diffuse transmittance measurements were done three times each with sample orientation randomized. Our integrating sphere data was processed in version 1 of the inverse adding-doubling (IAD) code[17] using four fluxes per iteration.
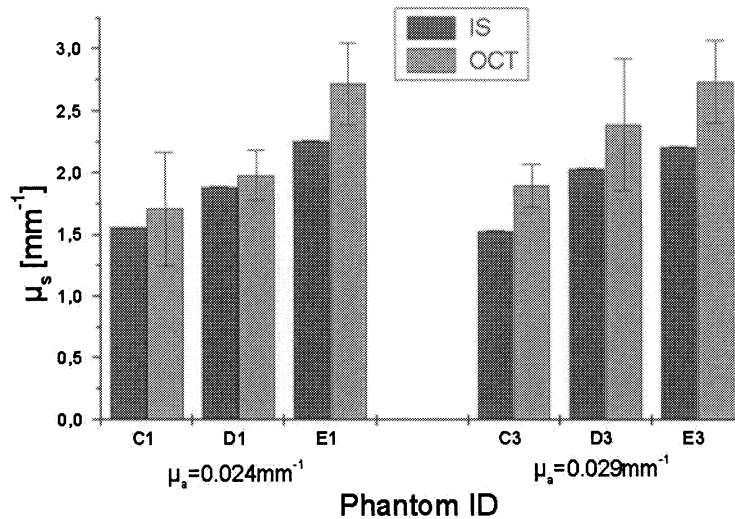
Fig. 4: A comparison of μ_s values (mean ± standard deviation) obtained from measurements on tissue phantoms with OCT extractions (green) and the integrating sphere (IS, red). Note the stepwise increase in μ observed in two separate sets of 3 phantoms purposely prepared to exhibit such an increase. Details about phantom nomenclature can be found in Ref. 18. Adopted from Ref. 5.

3.3 Fitting routine

Each phantom was imaged twice, with the light focused on the phantom surface in all cases. The OCT data was evaluated in the following manner: In every image there were five ROIs with fifteen curve fitting attempts per ROI. Curve fitting attempts in a single ROI only differed by the combinations of μ_s and θ_{rms} guesses used. A random number generator determined the transverse boundary pixels for each ROI. The fitted length was chosen to be 0.77 mm (186 pixels), the maximum that could be used in all the images accounting for phantoms imaged at a small angle. Phantoms whose optical depth (i.e., μ_s × scattering layer thickness) did not exceed 1.3 as determined with the integrating sphere and thus did not definitively enter the multiple-scattering regime were excluded.

3.4 Results and Discussion

A graphical comparison of μ_s obtained from OCT extractions and from the IAD code is shown in Fig. 4. Error bars representing the standard deviation on the measurements are not readily visible on the sphere data since the standard deviation did not exceed 0.25% of the mean. A Mie calculation using the code from Bohren & Huffman for homogeneously shaped spherical particles[4] was performed to obtain a theoretical $g_{eff} = 0.885$. A comparison of g_{eff} derived from OCT extractions to the theoretical result is shown in Fig. 5.

As shown in Figs. 4 and 5, the extraction algorithm generated consistent and reliable results for the tissue phantoms investigated. Every value of g_{eff} extracted overlapped with the 0.885 obtained from the Mie calculation within the error bars (Fig. 5). Moreover, a step-wise increase in μ_s was clearly observed with two different phantom sets (3 phantoms/set) using *both* techniques. While the error bars in three of six phantoms overlapped with the value returned from the IAD algorithm, the difference in the remaining three did not exceed 13% of the IAD returned value. One can notice, however, that the OCT-technique seems to slightly overestimate the scattering coefficient for these particular samples.

In examining the potential sources of error in the OCT extractions, the following should be considered: The integrating sphere measures optical properties of scattering media on a macroscopic scale as an average throughout the sample, while optical property extractions from an OCT image involves averaging over a much smaller region. Thus, inevitable phantom inhomogeneities on a μm scale could have affected our results. Also, IAD does not take wavelength as one of its inputs[17], or in other words, is designed for monochromatic light where samples exhibit uniform optical properties. The source used in this experiment had a 3 dB bandwidth of 60 nm, which could have an influence on the experiments and thus the returned IAD data. Furthermore, phantom albedos (~0.97) were slightly outside the recommended range of 0.4-0.95 for achieving the highest accuracy with the IAD algorithm[19], and this too could have slightly offset the IAD data points.

Considering the fine overall agreement between extracted values using our new algorithm and the IAD algorithm, we conclude that our new algorithm is capable of extracting optical properties with sufficient reliability.
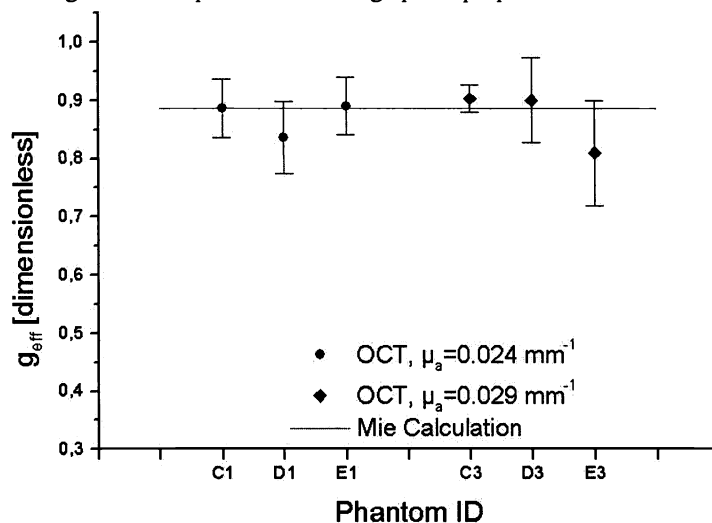

Fig. 5: A comparison of g_{eff} value (mean ± standard deviations) from OCT extractions (points) and the Mie calculation (line). Overlap in results is observed for every phantom. Details regarding phantom nomenclature can be found in Ref. 18. Adopted from Ref. 5.

4. SINGLE-LAYER *EX VIVO* STUDY

Recently, OCT has shown promise for imaging of coronary atherosclerotic plaques.[20,21] At present, however, visual differentiation between the general histopathological types of plaques, i.e., fibrous, fibrocalcific, and lipid-rich lesions, in OCT images is inherently qualitative and subjective. Several features of atherosclerotic plaque histopathology, i.e., reorganization and disruption of intimal collagen fibers, are expected to produce marked changes in the tissue optical scattering properties (μ_s and g_{eff}). Thus, to exemplify how our OCT algorithm may provide quantitative information about complex tissue pathology, we performed a preliminary *ex vivo* investigation in human atherosclerotic lesions.
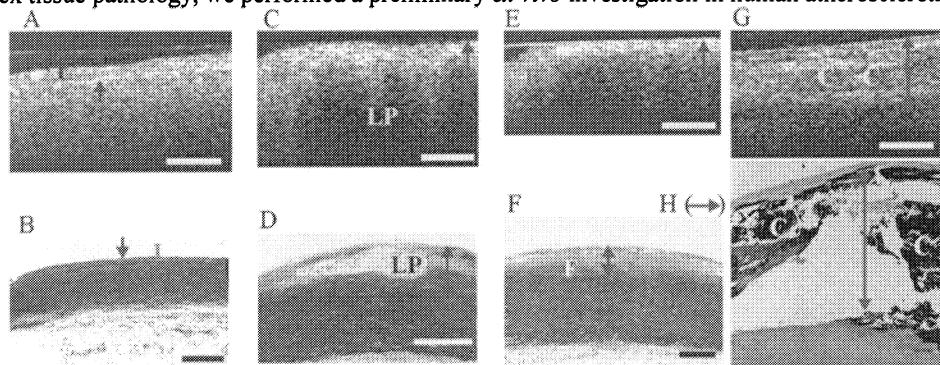

Fig. 6: Correlation of raw OCT images (A, C, E, and G) and histopathology (B, D, F, and H). Normal intima labeled 'I' in (A-B). Lipid-rich lesion (C-D), with a lipid pool marked 'LP'. Fibrous plaque (E-F), with fibrous area marked 'F'. Fibrocalcific lesion (G-H), with the calcifications denoted 'C'. Rupture artifacts caused by the decalcifying process are clearly seen in (H). The arrows represent the intima in (A-F) and the fitting region in (G-H), respectively. Bars=500 μm. Adopted from Ref. 5.

4.1 Curve fitting and imaging

Fourteen (4 normal, 4 lipid-rich, 3 fibrous, and 3 fibrocalcific) aortic segments were obtained within four hours of autopsy and imaged with OCT in phosphate buffered saline. During OCT imaging, the OCT probe was in contact with a glass cuvette inside of which the biopsies were mounted. Regions corresponding to those imaged by OCT were marked and located on digital photos. The samples were routinely paraffin-embedded and sliced at the regions defined by the

digital photographs. Sections were stained (hematoxylin and eosin or combined elastin and van Gieson Hansen staining) and corresponding areas of the intima were identified in OCT images and histological sections, respectively, using Table 1 in Ref. 20 as a guide. The OCT images were laterally divided into ROIs spanning approximately 20-30 A-scans or 200-300 μm. Altogether, the images were subdivided into 151 ROIs, including 41 normal, 40 lipid-rich, 34 fibrous, and 36 fibrocalcific ROIs, with each ROI being systematically selected for the criterion of the ROI spanning an area with uniform scattering properties. To facilitate interpretation, the extracted data were grouped into intervals based on the respective values of μ_s and g_{eff}. For μ_s, the intervals spanned 5 mm^{-1} for values from 0 to 40 mm^{-1}, and 10 mm^{-1} for values over 40 mm^{-1}. Since human soft tissue is generally very forward scattering, g_{eff} range intervals of 0.05 were chosen for g_{eff} values near 1, but the interval range was larger for the limited number of g_{eff} values below 0.8.

(A)
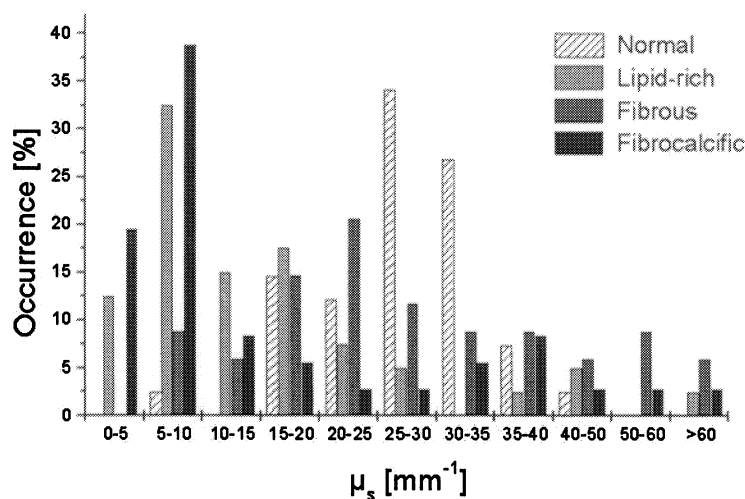
(B)
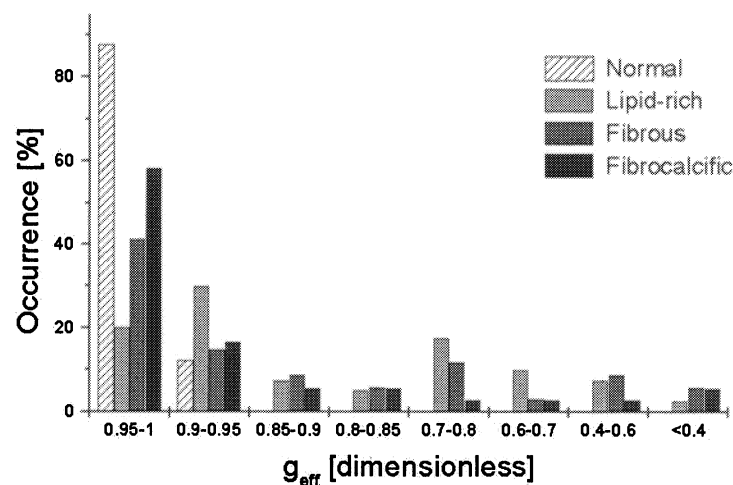

Fig. 7: Distributions of μ_s (A) and g_{eff} (B) for normal arteries and lipid-rich, fibrous, and fibrocalcific atherosclerotic plaques, respectively. In (A), μ_s for normal samples (striped) were centered between 15 and 40 mm^{-1}, but were centered at lower values for lipid-rich (green) and fibrocalcific (blue) plaques, and were randomly distributed for fibrous plaques (red). In (B), g_{eff} values were generally higher in normal intimas than in atherosclerotic lesions. Adopted from Ref. 5.

4.2 Initial results

OCT images were correlated with the corresponding histological sections using Table 1 in Ref. 20 as a guide and representative samples are shown in Fig. 6. Qualitatively, images obtained by OCT and microscopy demonstrated similar gross histopathological features that allowed for reasonable differentiation between normal vessels and lipid-rich, fibrous, and fibrocalcific plaques, respectively. The distribution of μ_s and g_{eff} for ROIs of normal arteries and the three overall atherosclerotic lesion types is shown in Fig. 7. Our preliminary data suggested that very similar optical properties were observed in images of normal samples (diagonal lines) but not in those representing atherosclerotic lesions. In normal arteries, almost 90% of g_{eff} values were concentrated between 0.95 and 1, whereas more than 50% of atherosclerotic lesion ROIs were below 0.95. Approximately 95% of the normal arterial samples had μ_s between 15 and 39 mm^{-1}, while μ_s was below 15 mm^{-1} in about 60% of lipid-rich and fibrocalcific plaques. Furthermore, fibrous lesions demonstrated very considerable variations in μ_s.

To our knowledge, the above preliminary data represent the first quantitative analysis of the optical scattering properties, i.e., the scattering coefficient and the anisotropy factor, of the normal and diseased human aortic intima *in vitro* at 1300 nm. The study indicates that the presented algorithm may provide a basis for extension of the OCT technique beyond qualitative image assessment towards tissue characterization based on physical principles. Techniques for detection of unstable atherosclerotic lesions have generated enormous interest in the field of vascular biology, and the future clinical utility of such methods is dependent on minimizing subjective and operator-dependent bias in the acquisition and interpretation of data[22]. We therefore suggest that the current OCT algorithm is an important step in this direction and that further studies are warranted to define the validity of the described method for characterization of atherosclerotic lesions.

5. VERIFICATION OF TWO-LAYER MODEL

Frequently, tissue (i.e., human blood vessels) is arranged in a multiple-layer geometry. Hence, to be clinically practical our OCT extraction algorithm needs to demonstrate its capability to extract optical properties from such geometry. In this section we show in a "proof of principle" numerical experiment that we were able to extract the optical properties μ_s and g_{eff} from a two-layer sample geometry. To do so, we first expanded Eqs. (1-4) of our model[9] to include a second layer for the sample arm geometry of interest (i.e., dynamic focusing), and hereby serve as an analytical EHF expression used for curve-fitting . We then present results from a numerical MC OCT experiment and the optical properties that were extracted using the analytical EHF model.

5.1 Extended model

In a multiple-layer geometry, the primary governing equation for the OCT signal remains Eq. (1). For the first layer, characterized by the optical parameters μ_{s1}, θ_{rms1}, and n_1, μ_s and z in Eq. (1) were replaced by μ_{s1} and z_1, respectively, where z_1 is the probing depth in the first layer. Under dynamic focusing conditions, the lateral coherence length $\rho_0(z)$ for this first layer[6,9] was then given by

$$\rho_{01}\left(z_1\right) = \sqrt{\frac{3}{\mu_{s1} z_1}} \frac{\lambda}{\pi \theta_{rms1}} \left[\frac{n_1 f}{z_1}\right],$$ (5)

where λ is the center wavelength of the source in vacuum, and f is the focal length of the sample arm focusing lens. For the second layer, characterized by μ_{s2}, θ_{rms2}, and n_2, z and $\mu_s z$ in Eq. (1) were replaced by z_2 and $\mu_{s1}\Delta_1 + \mu_{s2}z_2$, respectively, where Δ_1 is the thickness of the first layer, and z_2 is the probing depth in the second layer. Furthermore, following the procedure outlined in Appendix A of Ref. 9, $\rho_0(z)$ for the second layer (with dynamic focusing) was derived[6]

$$\rho_{02}\left(z_2\right) = \frac{\sqrt{3}}{\pi} \sqrt{\frac{\left\{\lambda n_2 \Delta_1 + \lambda n_1 \left[z_2 + n_2 \left(f - \frac{\Delta_1}{n_1} - \frac{z_2}{n_2}\right)\right]\right\}^2}{n_2^2 \Delta_1 \left(\Delta_1^2 + 3\Delta_1 z_2 + 3z_2^2\right)\theta_{rms1}^2 \mu_{s1} + n_1^2 z_2^3 \theta_{rms2}^2 \mu_{s2}}}.$$ (6)

5.2 Results and Discussion

Without loss of generality, the refractive indices of the sample and the surroundings were matched and approached unity. The system parameters in this case were λ = 800 nm, w_o = 0.4 mm, and f = 8.0 mm. The first layer was 0.3 mm thick (Δ_1) with μ_{s1} = 5.0 mm^{-1} and g_1 = 0.99. The second layer was 0.9 mm thick with μ_{s2} = 10.0 mm^{-1} and g_2 = 0.92. The MC

simulation of the mean square heterodyne signal current is shown as squares in Fig. 8. Because the MC data was normalized to unity at $z_1 = 0$ mm in the present case, $\langle i^2 \rangle_0$ was kept constant and equal to unity for the first layer, but served as a fitting parameter for the second layer. The fit of the two-layer EHF OCT model to the MC simulation is shown as a solid line in Fig. 8, and the extracted optical scattering parameters μ_s and g_{eff} of the two layers are shown in Table 1 together with the input parameters of the MC simulation. For completeness, results for other cases with different scattering coefficients μ_{s2}, but all other parameters unchanged, were included in Table 1. The absolute relative differences between the extracted mean values and the values used in the MC simulation followed a kind of structured pattern with increasing values of μ_{s2}, and the "true" values were not contained within the estimated standard deviations. This observation is a clear indication of a bias between the EHF model and the MC simulations. On the other hand, the small relative differences demonstrated the capability of the EHF OCT model to extract optical scattering parameters from multi-layered tissue, i.e., *in vivo* human blood vessels. In general, the index of refraction of each layer may also be extracted, but such analysis was outside the scope of the current paper.
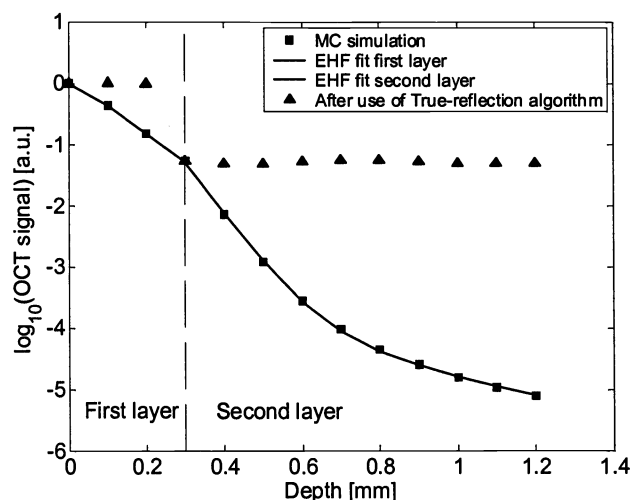

Fig. 8: MC simulation of the OCT signal for a two-layer sample with $\mu_{s2} = 10.0$ mm^{-1} (squares). EHF fit to the first and second layers (solid line). MC simulation of the OCT signal according to the true-reflection algorithm (triangles). Adopted from Ref. 6.

Notice that μ_s and g_{eff} could only be separated when the optical depth was sufficiently large for multiple scattering to occur. In general, when the optical depth was small, only single scattering occurred and therefore only μ_s could be extracted. For very large optical depths, i.e., totally diffused light, the EHF model predicted the OCT signal to be determined by the reduced scattering coefficient and, μ_s and g_{eff} could therefore not be separated using this model alone.

In addition to providing quantitative information about the tissue, the extracted optical properties may also be used for attenuation compensation in OCT images, i.e., to remove attenuation caused by scattering and improve differentiation between tissue types.[23] Such an attenuation correction technique (also called "true-reflection OCT algorithm"[23]) can be easily implemented with use of the fitted coefficients from both layers and Eq. (1). The MC simulation of the OCT signal after correction for the attenuation caused by scattering is shown as triangles in Fig. 8. The distinct signal levels obtained for the two different layers after using the true-reflection algorithm strongly indicate that better differentiation of different tissue types may be obtained in OCT images of real tissue by using the true-reflection algorithm. This too is expected to result in an improved diagnosis.

Table 1. Input parameters of the MC simulation and the extracted parameters obtained by using the EHF model, respectively, with the relative difference expressed in % . Leave-one-out cross-validation[24] with respect to the MC data points was used to estimate the standard deviations. Adopted from Ref. 6.

Layer	MC input μ_s [mm^{-1}]	Extracted μ_s [mm^{-1}]	Rel. diff. [%]	MC input g_{eff} -	Extracted g_{eff} -	Rel. diff. [%]
1	5.000	4.98 ± 0.05	-0.4	0.9900	0.974 ± 0.007	-1.6
2	4.000	4.4 ± 0.1	10	0.9200	0.940 ± 0.003	2.2
2	6.000	6.3 ± 0.1	5.0	0.9200	0.893 ± 0.003	-2.9
2	8.000	8.2 ± 0.1	2.5	0.9200	0.874 ± 0.005	-5.0
2	10.00	9.9 ± 0.2	-1.0	0.9200	0.864 ± 0.006	-6.1

6. CONCLUSIONS

In conclusion, we have developed and validated a novel method to perform extraction of optical scattering parameters, i.e., the scattering coefficient μ_s and effective anisotropy parameter g_{eff}, in OCT images. In the single-layer phantom study, we showed that OCT was capable of accurately determining the optical scattering properties of highly scattering media, and we obtained results that were in agreement with a well-established experimental method. Using this technique, we conducted for the first time to our knowledge a preliminary investigation that quantitatively compared the optical scattering properties of the human arterial intima *ex vivo*. These preliminary data indicated that differences in scattering properties data exist between normal and atherosclerotic arterial segments and optical scattering data provided by OCT can therefore potentially contribute to atherosclerotic plaque characterization. Finally, with the two-layer phantom study we demonstrated that our two-layered model could accurately describe the OCT signal, extract the optical properties, and correct for attenuation losses in a two-layered tissue structure. The current study demonstrated that with use of the outlined algorithm, the optical scattering properties of single- and multi-layered tissue can be characterized from OCT images. The OCT analysis presented here can open new avenues of OCT research by combining high-resolution tissue imaging with measurements of tissue optical scattering properties. Such analysis may allow for assessment of yet unexplored biophysical properties of tissues and holds considerable promise for future clinical utility.

ACKNOWLEDGEMENTS

[1] D. Huang, E. A. Swanson, C. P. Lin, J. S. Schuman, W. G. Stinson, W. Chang, M. R. Hee, T. Flotte, K. Gregory, C. A. Puliafito, and J. G. Fujimoto, "Optical coherence tomography," Science **254**, 1178 (1991).

[2] B. Povazay, K. Bizheva, A. Unterhuber, B. Hermann, H. Sattmann, A. F. Fercher, W. Drexler, A. Apolonski, W. J. Wadsworth, J. C. Knight, P. S. J. Russel, M. Vetterlein, and E. Scherzer, "Submicrometer axial resolution optical coherence tomography," Opt. Lett. **27**, 1800-1802 (2002).

[3] G. J. Tearney, S. A. Boppart, B. E. Bouma, M. E. Brezinski, N. J. Weissman, J. F. Southern, and J. G. Fujimoto, "Scanning single-mode fiber optic catheter-endoscope for optical coherence tomography," Opt. Lett. **21**, 543 (1996).

[4] C. F. Bohren and D. R. Huffman, *Absorption and scattering of light by small particles* (John Wiley & Sons, Inc., New York, NY 1983).

[5] D. Levitz, L. Thrane, M. H. Frosz, P. E. Andersen, C. B. Andersen, J. Valanciunaite, J. Swartling, S. Andersson-Engels, and P. R. Hansen, "Determination of optical scattering properties of highly-scattering media in optical coherence tomography images," Opt. Express **12**, 249 (2004).

[6] L. Thrane, M. H. Frosz, T. M. Jørgensen, A. Tycho, H. T. Yura, and P. E. Andersen, "Extraction of optical scattering parameters and attenuation compensation in optical coherence tomography images of multilayered tissue structures," Opt. Lett. **29**, 1641 (2004).

[7] A. Tycho, T. M. Jørgensen, H. T. Yura, and P. E. Andersen, "Derivation of a Monte Carlo method for modeling heterodyne detection in optical coherence tomography systems," Appl. Opt. **41**, 6676 (2002).

[8] R. F. Lutomirski and H. T. Yura, "Propagation of a finite optical beam in an inhomogeneous medium," Appl. Opt. **10**, 1652-1658 (1971).

[9] L. Thrane, H. T. Yura, and P. E. Andersen, "Analysis of optical coherence tomography systems based on the extended Huygens-Fresnel principle," J. Opt. Soc. Am. A **17**, 484 (2000).

[10] A. E. Siegman, *Lasers* (University Science Books, Mill Valley, CA 1986).

[11] H. T. Yura, L. Thrane, and P. E. Andersen, "Closed form solution for the Wigner phase-space distribution function for diffuse reflection and small angle scattering in a random medium," J. Opt. Soc. Am. A **17**, 2464-2474 (2000).

[12] C. C. Cheng and M. G. Raymer, "Propagation of transverse optical coherence in random multiple-scattering media," Phys. Rev. A **62**, 1-12 (2000).

[13] G. J. Tearney, B. Bouma, and J. G. Fujimoto, "High-speed phase- and group-delay scanning with a grating-based phase control delay line," Opt. Lett. **22**, 1811-1813 (1997).

[14] A. M. Rollins and J. A. Izatt, "Optimal interferometer designs for optical coherence tomography," Opt. Lett. **24**, 1484-1486 (1999).

[15] J. M. Schmitt, A. Knüttel, and R. F. Bonner, "Measurement of optical properties of biological tissues by low-coherence reflectometry," Appl. Opt. **32**, 6032 (1993).

[16] L. H. Wang, S. L. Jacques, and L. Q. Zheng, "MCML – Monte Carlo modeling of light transport in multilayered tissues," Computer Methods Programs Biomed. **47**, 131 (1995).

[17] S. A. Prahl, Inverse Adding-Doubling Software. 1999. http://omlc.ogi.edu/software/iad/index.html.

[18] J. Swartling, J. S. Dam, and S. Andersson-Engels, "Comparison of spatially and temporally resolved diffuse-reflectance measurement systems for determination of biomedical optical properties," Appl. Opt. **42**, 4612-4620 (2003).

[19] D. D. Royston, R. S. Poston, and S. A. Prahl, "Optical properties of scattering and absorbing materials used in the development of optical phantoms at 1064 nm," J. Biomed. Opt. **1**, 110-116 (1997).

[20] I. K. Jang, B. E. Bouma, D. H. Kang, S. J. Park, S. W. Park, K. B. Seung, K. B. Choi, M. Shishkov, K. H. Schlendorf, E. Pomerantsev, S. L. Houser, H. T. Aretz, and G. J. Tearney, "Visualization of coronary atherosclerotic plaques in patients using optical coherence tomography: comparison with intravascular ultrasound," J Am Coll Cardiol **39**, 604-609 (2002).

[21] H. Yabushita, B. E. Bouma, S. L. Houser, H. T. Aretz, I. K. Jang, K. H. Schlendorf, C. R. Kauffman, M. Shishkov, D. H. Kang, E. F. Halpern, and G. J. Tearney, "Characterization of human atherosclerosis by optical coherence tomography," Circulation **106**, 1640-1645 (2002).

[22] Z. Fayad and V. Fuster, "Clinical imaging of the high-risk or vulnerable atherosclerotic plaque," Circ. Res. **89**, 305-316 (2001).

[23] L. Thrane, T. M. Jørgensen, P. E. Andersen, and H. T. Yura, "True-reflection OCT imaging," Proc. SPIE **4619**, 36 (2002).

[24] M. Stone, "Cross-validation choice and assessment of statistical predictions," J. Royal. Statzs. Soc. **B36**, 111 (1974).